Journal of Southeast University (English Edition) Vol. 40, No. 3, pp. 286 - 294 Sept. 2024 ISSN 1003—7985

Micropores in G20Mn5N cast steel and their influence on stress distribution

Yan Huadong Jin Hui

(School of Civil Engineering, Southeast University, Nanjing 211189, China)
(Jiangsu Key Laboratory of Engineering Mechanics, Southeast University, Nanjing 211189, China)

Abstract: To accurately analyze the impact of casting pores in steel, high-resolution 3D X-ray tomography technology was used to gather detailed statistical information about micropores. These micropores were classified as gas, shrinkage, and gas-shrinkage pores depending on their formation origin and morphology. Clustering tendencies and affinity parameters were defined to characterize the spatial correlations among these three types of pores. The 3D data from X-ray tomography scans were then integrated into finite element analysis (FEA) software to predict how micropore shape, size, and distribution influence stress distribution within the material. The results show that certain inflection points with small local radii within the cast pores are major contributors to stress concentration. Therefore, cast pores cannot be simply modeled as ideal spherical pores. The sphericity and volume of pores have a significant impact on the stress concentration of the model. Specifically, lower sphericity and larger pore volumes result in higher stress concentrations. Moreover, the internal pores of steel castings exhibit specific global distribution characteristics. Pores located on the surface of the specimen lead to significantly higher stress concentrations compared to those located inside the specimen.

Key words: cast steel; micropores; X-ray tomography; 3D reconstruction; finite element analysis
DOI: 10.3969/j.issn.1003-7985.2024.03.008

Cast steel is extensively used in civil engineering structures owing to its excellent strength, toughness, and impact resistance. Sand casting is the preferred manufacturing process for many applications involving low-alloy cast steel[1]. However, various production processes such as casting design, molding sand, welding repair, and heat treatment can introduce certain micro defects in steel castings[2-3]. These micro defects can cause discontinuities in the cast steel, adversely affecting steel casting durability[4-6].

Received 2023-11-06, **Revised** 2024-02-29.

Biographies: Yan Huadong (1990—), female, doctor; Jin Hui (corresponding author), female, doctor, professor, jinhui@seu.edu.cn.

Foundation item: The National Natural Science Foundation of China (No. 51578137).

Citation: Yan Huadong, Jin Hui. Micropores in G20Mn5N cast steel and their influence on stress distribution[J]. Journal of Southeast University (English Edition), 2024, 40(3): 286 - 294. DOI: 10.3969/j.issn.1003-7985.2024.03.008.

A typical type of micro defects in cast steel is micropores, which can be classified into gas pores, shrinkage pores, and gas-shrinkage pores based on their formation origins[7-8]. Gas pores are formed owing to dissolved gases. Gas solubility in solid metals is much lower than that in liquid metals. Therefore, as the metal cools and solidifies, gas solubility decreases, causing gas bubbles to form. Shrinkage pores result from hindered liquid flow, preventing proper volume change during solidification. The interaction between gas dissolution and metal shrinkage causes the formation of gas-shrinkage pores.

To evaluate the impact of these defects on the ductility and strength of steel castings, numerous experimental and numerical modeling studies have been conducted. The different morphologies and size ranges of gas, shrinkage, and gas-shrinkage pores correlate differently with ductility and strength, requiring a quantitative characterization of these defect parameters to accurately predict the mechanical properties of cast steel components. For instance, Gao et al.[9] developed a finite element model to analyze the effect of porosity on the mechanical performance of cast aluminum silicon, though their model was derived from 2D metallography observations. Li et al.[10] predicted the effect of 3D pores on the mechanical properties of the aluminum alloy A356 but overlooked the highly irregular shapes of casting pores. Consequently, the study focused on cast pore reconstruction and conducted a finite element analysis (FEA). Recent developments in X-ray tomography have provided in situ observations and 3D characterizations of porosity[11-14]. In addition, numerical simulation methods based on X-ray images have been used to validate experimental observations and further understand how microstructure influences mechanical performance[15-18].

This study aims to quantify and characterize the 3D morphologies, size distributions, and spatial arrangements of gas, shrinkage and gas-shrinkage pores in cast steel. Subsequently, a representative volume element (RVE) containing different distributions, sizes and shapes of casting pores is developed to determine the relationship between these and the mechanical behavior of the material.

1 Materials and Methods

1.1 Materials

The cast steel material studied in this paper is G20Mn5N, which exhibits a yield strength of 320 MPa and a tensile strength of 600 MPa at room temperature. The specimens used in the experiment were extracted from a casting ingot with dimensions of 250 mm × 180 mm × 60 mm. The macroscopic mechanical properties of G20Mn5N were considered isotropic during the tensile test. All samples were uniform in dimension, as illustrated in Fig. 1, with a thickness of 2 mm.

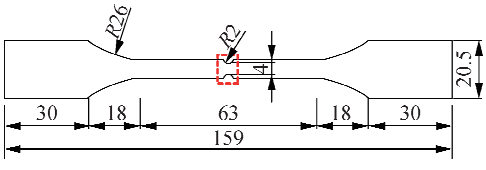

Fig. 1 Notched tensile sample[7] (unit: mm)

1.2 X-ray tomography observations

For the analysis, notched specimens were scanned using a Y. CT Precision System industrial tomography scanner. This system features a 225-kV X-ray source with a minimum focal spot size of 5 μm and a Perkin Elmer XRD 0820 16-bit amorphous silicon sensor, equipped with a flat-panel detector producing images with a resolution of 1 024 × 1 024 pixels. The source-to-detector distance was 204 mm. Overall, 1 350 projections were recorded by the detector. The X-ray computed tomography (XCT) images were reconstructed from these projections using a cone and beam back-projection algorithm. All samples were scanned under identical measurement conditions. To achieve maximum measurement resolution, only the center of each sample (dashed line in Fig. 1) was reconstructed. Specific scanning parameter settings can be found in Refs. [7, 19].

The obtained data were processed using advanced 3D voxel analysis and visualized with the software package VG-Studio Max 3.0. Pore segmentation within the specimens was evaluated using global and local gray value thresholds.

2 Analyses of Results

In this study, we analyzed the quantity, size, and morphology of gas, shrinkage, and gas-shrinkage micropores in cast steel. Pore size and shape were characterized using the effective diameter d and the sphericity C[17]. Here, d denotes the diameter of the equivalent sphere that has the same volume as the defect, and C represents the ratio of the surface area of a sphere (with the same volume as the defect volume) to the actual surface areas of the defect.

$$d = \sqrt[3]{\frac{6V}{\pi}} \tag{1}$$

$$C = \sqrt[3]{\frac{36\pi V^2}{s^3}} = \frac{\sqrt[3]{36\pi V^2}}{s} \tag{2}$$

where V and s are the actual volume and surface area of the pore, respectively.

2.1 Morphological characteristics of micropores

Table 1 summarizes the pore analysis for samples 1-9. Pore sizes were calculated based on their volumes. For all specimens, the minimum detectable volume was 7×10^{-5} mm^3. Pores with volumes of less than 20 voxels were excluded from the analysis owing to significant measurement noise and artifacts. A total of 2 726 pores were detected across the 9 samples, with an average volume of 3.7×10^{-4} mm^3, an average surface area of 0.045 mm^2, and an average sphericity of 0.546. The highest volumetric porosity was found in sample 4, reaching nearly 0.500%, whereas sample 2 exhibited the lowest porosity at approximately 0.156%. Maximum pore volumes varied among specimens, ranging from 0.046 5 mm^3 in sample 4 to 3.42×10^{-3} mm^3 in sample 2. Fig. 2 shows the 3D distribution of micropores along the gauge length of four samples.

Table 1 Information statistics of micropores in the nine samples (average value)[7, 19]

Sample	Number	Fraction/%	Volume/10^{-4} mm^3	Surface area/10^{-2} mm^2	Effective diameter/mm	Sphericity
1	184	0.176	2.5	3.470	3.628	0.469
2	192	0.156	3.7	4.776	4.135	0.508
3	492	0.327	2.7	3.799	3.723	0.471
4	398	0.484	5.4	5.698	4.690	0.493
5	420	0.373	2.5	3.492	3.628	0.495
6	331	0.276	3.5	4.374	4.059	0.519
7	151	0.184	4.3	5.168	4.347	0.516
8	368	0.307	3.7	4.578	4.135	0.526
9	190	0.300	6.2	6.263	4.911	0.510

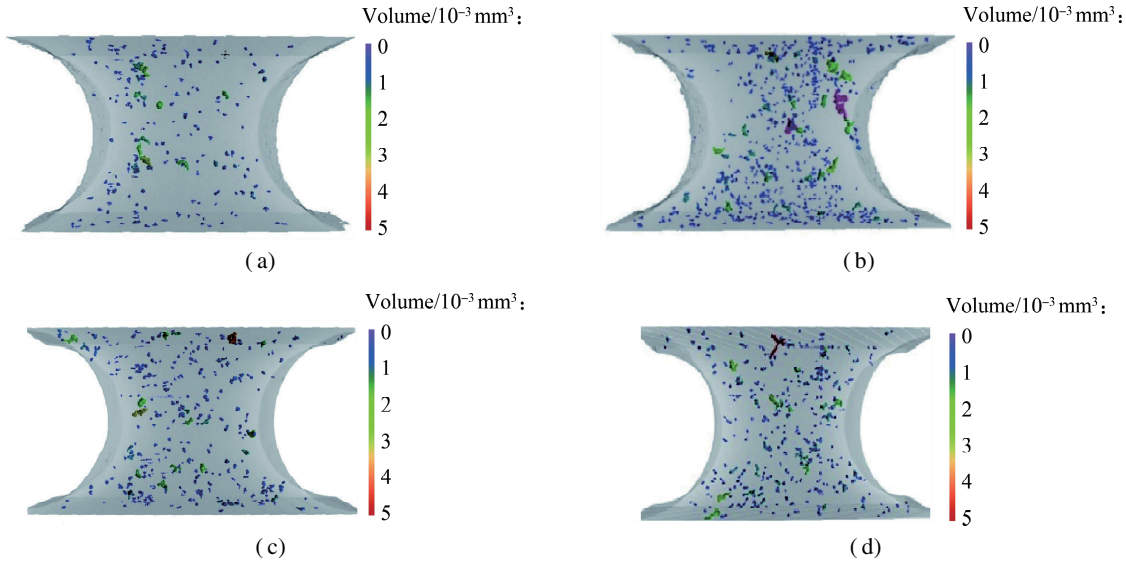

Fig. 2 Micropores inspected with 3D X-ray tomography technology in the sample gauge section. (a) Sample 1; (b) Sample 5; (c) Sample 6; (d) Sample 8[7, 19]

The micropores were classified into three types based on their formation origins and morphological characteristics: gas, gas-shrinkage, and shrinkage pores. Table 2 compares the information for each type of micropore, while Fig. 3 displays the typical morphology of each type.

Table 2 Information on gas, gas-shrinkage, and shrinkage pores[7, 19]

Type	Number	Volume/10 $^{-4}$ mm^3			Surface area/mm^2			Mean effective diameter/mm	Mean sphericity
		Max	Min	Mean	Max	Min	Mean		
Gas pore	1 407	33.3	0.7	2.2	0.197 3	0.111 8	0.299 2	3.48	0.59
Gas-shrinkage pore	1 189	37.7	0.7	3.5	0.289 4	0.161 0	0.510 4	4.06	0.47
Shrinkage pore	130	464.8	1.0	21.7	0.278 4	0.281 8	0.231 2	7.46	0.35

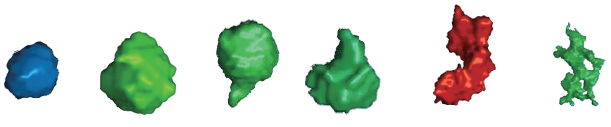

Fig. 3 Morphologies and characteristics of representative micropores in the samples. (a) Gas pores; (b) Gas-shrinkage pores; (c) Shrinkage pores[7, 19]

Gas pores were the most prevalent, accounting for 51.61% of all detected pores. Despite being fewer in number, shrinkage pores had the largest average volume, 9.86 times higher than that of gas pores and 6.20 times higher than that of gas-shrinkage pores. However, the total volume of shrinkage pores was the smallest among the pore types owing to their lower frequency. As depicted in Fig. 3, shrinkage pores tend to be more irregular and flat, gas pores are more spherical, and gas-shrinkage pores exhibit characteristics between these two; the equivalent diameter of shrinkage pores is the largest, but their average sphericity is the lowest.

2.2 Distribution statistics of micropores

Micropore size in cast steel is essential for analyzing pore formation and understanding the impact of pores on the material's mechanical properties[20]. This paper uses a logarithmic normal distribution function to statistically analyze the micropore distribution in G20Mn5N. The two-parameter lognormal statistics function is expressed in Eq. (3), and the three-parameter lognormal statistical function is shown in Eq. (4)[21].

$$f(x) = \frac{1}{x\sigma\sqrt{2\pi}}\exp\left[\frac{-(\ln x-\mu)^2}{2\sigma^2}\right] \tag{3}$$

$$g(x) = \frac{1}{(x-\tau)\sigma\sqrt{2\pi}}\exp\left[\frac{-(\ln(x-\tau)-\mu)^2}{2\sigma^2}\right] \tag{4}$$

where μ is the logarithmic mean value; σ is the standard deviation; and τ signifies the threshold.

The μ and σ values in Eq. (3) were estimated using the measured pore size data. Once τ is determined, the logarithmic average and standard deviation in Eq. (4) can be deduced by applying similar statistical principles as those used in Eq. (3).

The fit of the pore size distribution can be tested using the Anderson-Darling statistic (Eq. (5)). The smaller the A^2 value, the better the fit.

$$A^2 = -n - \frac{1}{n}\sum_{i=1}^{n}(2i-1)[\log(P(x_i)) + \log(1-P(x_{n-i+1}))] \tag{5}$$

where n is the number of pores to be fitted; i represents the order of pores arranged by volume from small to

large; and $P(x_i)$ denotes the cumulative probability.

Fig. 4 presents the fitting results of Eqs. (3) and (4), while Table 3 summarizes the fitting parameters. The A^2 value for the three-parameter lognormal distribution is 35.15, which is significantly lower than the A^2 value of 119.45 for the two-parameter lognormal distribution. This indicates that the pore diameter of G20Mn5N cast steel follows a three-parameter lognormal distribution. The diameter threshold for all micropores was found to be 62.23 μm, meaning that the minimum pore diameter detected in G20Mn5N cast steel is 62.23 μm.

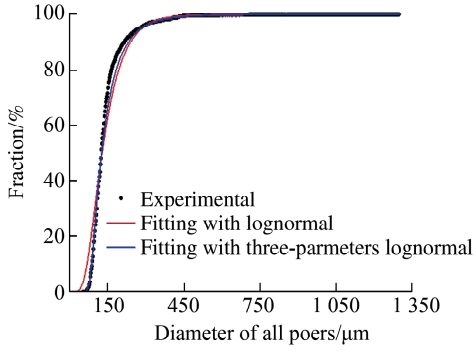

Fig. 4 Fitting results of cumulative diameter

Table 3 Fitting parameters for the two distributions

Lognormal			3-parameter lognormal			
μ	σ	A^2	μ	σ	τ	A^2
4.844 68	0.488 86	119.45	4.144 78	0.759 58	62.227 81	35.15

2.3 Clustering tendency of the micropores

The nearest-neighbor distribution can aid in quantifying important aspects of the spatial arrangement of gas, gas-shrinkage, and shrinkage pores. To estimate this distribution, the centroid coordinates (X, Y, Z) of all pores in the structural field must be measured. Let n be the total number of pores in the structural frame, and let (X_1, Y_1, Z_1), (X_2, Y_2, Z_2), …, (X_i, Y_i, Z_i), …, (X_n, Y_n, Z_n) represent the centroid coordinates of these n pores. This simple function $D = ((X_j - X_k)^2 + (Y_j - Y_k)^2 + (Z_j - Z_k)^2)^{1/2}$ can be used to calculate the distance between the j-th pore and the k-th pore. This calculation can be repeated for all pores with known centroid coordinates. Using these data, a frequency histogram of the nearest-(or higher-order) neighbor distances can be generated in a straightforward manner. Fig. 5 illustrates the nearest-neighbor distance distributions of the gas, gas-shrinkage, and shrinkage pores. The average nearest-neighbor distances for gas, gas-shrinkage, and shrinkage pores are 326.1, 323.8, and 413.7 μm, respectively.

To quantify the clustering tendency of the micropores and test the divergence of the observed distribution from complete randomness[22], a clustering parameter P is defined. This parameter is the ratio of the observed mean

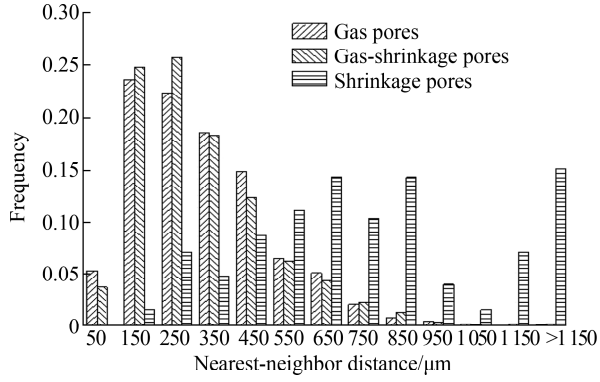

Fig. 5 Nearest-neighbor distance distributions

nearest-neighbor distance between pores D_o to the corresponding nearest-neighbor distance D_r for randomly distributed pores of the same quantity, density, volume fraction, and size distribution. The expression of P is given as follows[5]:

$$P = \frac{D_o}{D_r} \tag{6}$$

Balasundaram et al.[22] used $D_r = 0.5\sqrt{V/N}$ to calculate the average nearest-neighbor distance for 2D randomly distributed pores. Given that the statistics in this paper rely on the 3D characteristics of pores, D_r should be obtained as follows:

$$D_r = 0.5\sqrt[3]{\frac{V}{N}} \tag{7}$$

where V is the volume of the structural field, and N is the number of pores.

The higher the value of P, the more pronounced the clustering tendency of the pores. A P value greater than 1.0 indicates a clustering nature, while a value less than 1.0 indicates a uniform nature. For these studied specimens, the clustering parameter P values were 1.01 for gas pores, 0.94 for shrinkage-gas pores, and 0.52 for shrinkage pores.

2.4 Correlation of different types of micropores

Pore arrangement and the correlation between different types of pores can be characterized by defining a paired nearest-neighbor distance. For example, the paired nearest-neighbor distribution function for gas and shrinkage pores represents the distance from a given gas pore to the nearest shrinkage pore. Fig. 6 shows the paired nearest-neighbor distance distributions between different types of pores, with $\bar{d}$ representing the average distance.

An affinity parameter $P_{a\text{-}b}$ that characterizes the affinity of pore type a to pore type b can be defined as follows[22]:

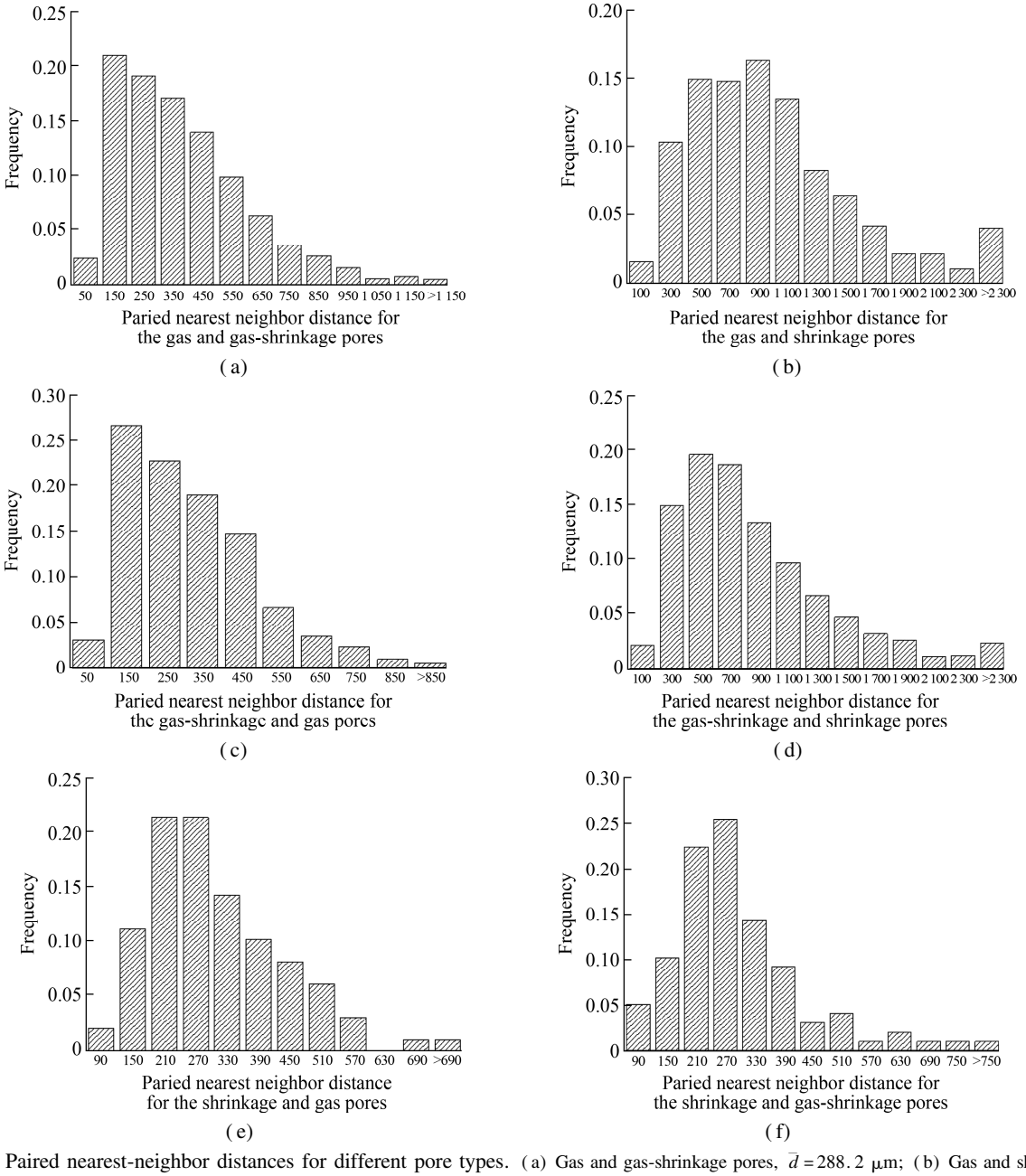

Fig. 6 Paired nearest-neighbor distances for different pore types. (a) Gas and gas-shrinkage pores, $\bar{d}=288.2$ μm; (b) Gas and shrinkage pores, $\bar{d}=1\,011.5$ μm; (c) Gas-shrinkage and gas pores, $\bar{d}=322.2$ μm; (d) Gas-shrinkage and shrinkage pores, $\bar{d}=880.6$ μm; (e) Shrinkage and gas pores, $\bar{d}=308.1$ μm; (f) Shrinkage and gas-shrinkage pores, $\bar{d}=298.3$ μm

$$P_{\text{a-b}}=\frac{D_{\text{a}}}{D_{\text{ab}}} \tag{8}$$

where D_{ab} is the average paired nearest-neighbor distance between pore types a and b, and D_{a} represents the average nearest-neighbor distance between type a pores only. A $P_{\text{a-b}}$ value greater than 1 implies that, on average, for a given type a pore, the nearest type b pore is closer than the nearest type a pore. The affinity parameters used in this study are listed in Table 4. In this table, $P_{\text{g-gs}}$ represents the affinity of gas and gas-shrinkage pores; $P_{\text{g-s}}$ denotes the affinity of gas and shrinkage pores; $P_{\text{gs-g}}$ is the affinity of gas-shrinkage and gas pores; $P_{\text{gs-s}}$ signifies the affinity of gas-shrinkage and shrinkage pores; $P_{\text{s-g}}$ indicates the affinity of shrinkage and gas pores; $P_{\text{s-gs}}$ is the affinity of shrinkage and gas-shrinkage pores.

Table 4 Pore affinity parameters of the G20Mn5N cast steel

$P_{\text{g-gs}}$	$P_{\text{g-s}}$	$P_{\text{gs-g}}$	$P_{\text{gs-s}}$	$P_{\text{s-g}}$	$P_{\text{s-gs}}$
0.84	0.32	1.00	0.37	1.34	1.39

3 Effect of Micropore Characteristics

To further understand and quantify the effects of pore characteristics (size, shape, and distribution) on the mechanical properties of cast steel, the 3D stress-strain distribution in a representative volume element (RVE) with dimensions of 0.6 mm × 0.6 mm × 0.6 mm was predicted using the general-purpose finite element package ABAQUS. The pores, reconstructed from 3D X-ray tomography images, were included in the RVE. The

main value of this approach lies in the use of actual 3D pore geometry rather than relying on either a 2D metallographic view of a pore or an idealized 3D model of a pore.

A quantitative parameter, k_σ, was proposed by Gao et al. [9] to account for the local concentrated stress:

$$k_\sigma = \frac{\sigma_{\max}}{\sigma_\infty} \tag{9}$$

where $\sigma_{\max}$ represents the maximum principal stress, and σ_∞ is the far-field stress.

3.1 Finite element modeling methodology

Building an RVE finite element model based on the actual 3D pore geometry involves three steps: 1) The pore X-ray tomography data with a slice thickness of 16 μm were saved in DICOM format. 2) Mimics software was used to convert the CT scanned image data from DICOM to STL format. The triangular mesh was then remeshed to reduce the number of low-quality triangles and to smooth the model. 3) ABAQUS was used to insert the pores as cavities into the RVE model and refine the mesh in the region surrounding the pores.

The elastoplastic constitutive formulation of G20Mn5N cast steel was modeled with a Young's modulus $E = 200$ GPa, a Poisson's ratio $\nu = 0.3$, and a yield stress $\sigma_y = 320$ MPa. The finite element type selected was C3D10M, a 10-node tetrahedron based on quadratic interpolation and a modified formulation. These second-order elements provide higher accuracy for complex stress fields than first-order elements. To determine the appropriate grid size, model J was partitioned using different grid sizes, namely 0.10, 0.05, 0.03, and 0.01 mm. The results showed significant variability with grid sizes of 0.10 and 0.05 mm, while grid sizes of 0.03 and 0.01 mm yielded consistent results. Therefore, a grid size of 0.03 mm was chosen for subsequent calculations.

For comparison, additional RVEs were created without pores and with idealized pore shapes. The details of these FE models are summarized in Table 5. FE models F, J, and K are shown in Fig. 7. A comparison of the pores in the RVE with those reconstructed from X-ray tomography images (see Fig. 7(b)) indicates a high level of accuracy in pore insertion.

Table 5 Information for different finite element models

Model	Pores			
	Number	Volume/ 10^{-3} mm^3	Sphericity	Type
B	1	0.65	1	Idealized
C	1	0.43	0.54	Gas
D	1	1.22	0.53	Gas
E	1	2.98	0.55	Gas
F	1	6.52	0.53	Gas-shrinkage
G	1	19.40	0.54	Gas-shrinkage
H	1	6.46	0.41	Gas-shrinkage
I	1	6.59	0.36	Shrinkage
J	1	3.10	0.37	Shrinkage
	2	3.44	0.42	Gas-shrinkage
K	1	1.27	0.52	Gas
	2	1.60	0.47	Gas-shrinkage
	3	3.86	0.38	Shrinkage

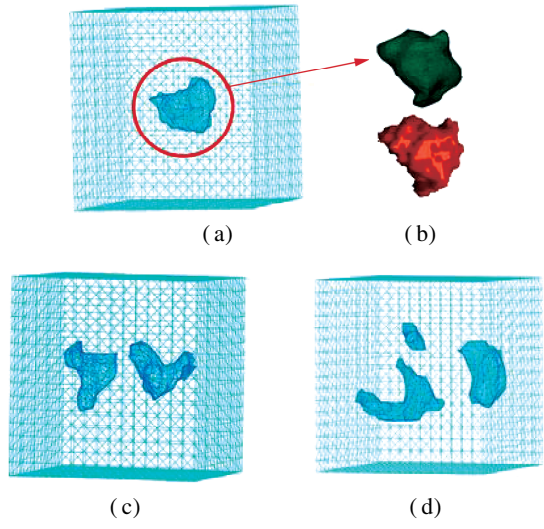

Fig. 7 FE model and pore geometry. (a) FE model F; (b) Comparison between reconstruction model and X-ray imaging model; (c) FE model J; (d) FE model K

3.2 Results of finite element simulations

3.2.1 Effect of pores

Finite element analysis was performed on the RVE model to evaluate the impact of pores on stress distribution. The global stress-strain distribution within a finite element model is largely influenced by its geometrical features; however, local variations can occur owing to stress concentrations around micropores. A smoothly varying stress field ranging from 300 to 330 MPa is observed in the pore-free RVE under applied stress. The maximum local stress is 330 MPa, slightly surpassing the yield stress of 320 MPa for G20Mn5N cast steel. This stress occurs at the center of the model. When pores are distributed in the RVE, then the stress concentration at this location increases.

3.2.2 Effect of the pore shape

The volume and the sphericity of pores, including those in the RVE, are employed to characterize the sizes and types of pores. The stress concentration fields were calculated for finite element models B, F, H, and I (see Table 5). These models featured pores with volumes ranging from 6.46×10^{-3} to 6.59×10^{-3} mm^3 but varied significantly in sphericity values: 1 for model B, 0.53 for model F, 0.41 for model H, and 0.36 for model I. Despite having almost identical volumes, pore shapes differed significantly. Fig. 8 shows the maximum principal stress distributions for these four models. The calculated stress concentration factors k_σ in models B, F, H, and I are 1.69, 4.32, 5.90, and 9.84, respectively.

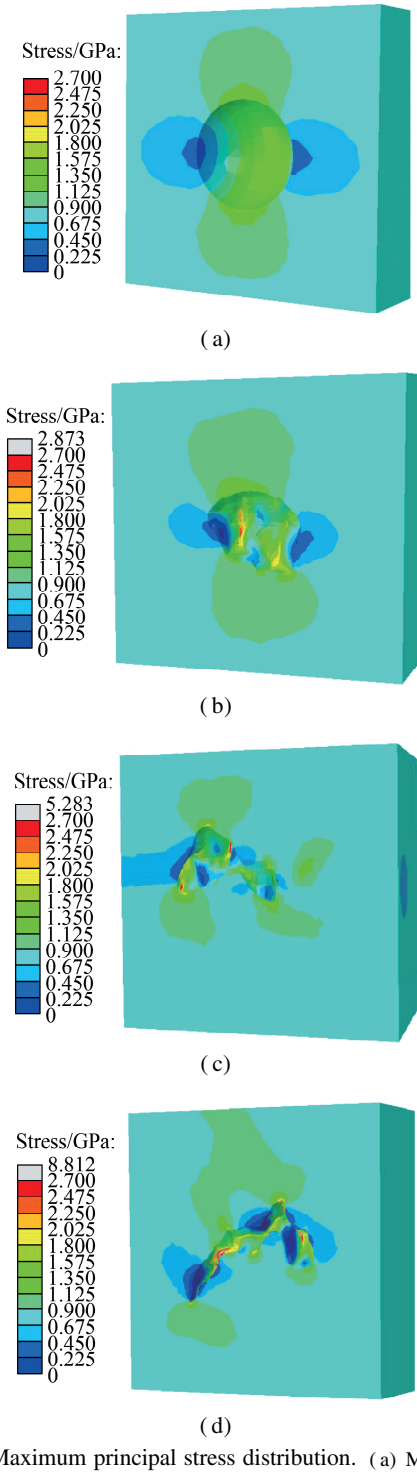

Fig. 8 Maximum principal stress distribution. (a) Model B; (b) Model F; (c) Model H; (d) Model I

Model B exhibited the lowest stress concentration coefficient of RVE, which was only 25.27% of the average stress concentration coefficient observed in models F, H, and I. This result underscores that microscopic pores with complex shapes cannot be approximated as ideal spheres when studying their effect on stress concentration. The sphericity of RVE models F, H, and I gradually decreases, while the stress concentration coefficient gradually increases. Therefore, pore sphericity greatly affects stress concentration. Specifically, lower sphericity in casting pores leads to higher stress concentration.

3.2.3 Effect of the pore size

The pores in FE models C, D, E, F, and G (see Table 5) had similar sphericities, but volumes varied greatly. Therefore, these five FE models can be used to analyze the effect of pore size on stress concentration. The stress concentration factors k_σ derived from FEAs are listed in Table 6 for all the cases examined.

Table 6 Stress concentration factor in the FE models

Model	C	D	E	F	G
k_σ	2.81	3.96	3.45	4.32	6.90

Among the RVE models C to G, model G exhibited the highest stress concentration coefficient, with a value of 6.90. This model also featured the largest pore volume at 1.94×10^{-2} mm^3, which was greater than the pore volumes in models C through F. Therefore, larger defect volumes result in pronounced stress concentrations.

3.2.4 Effect of the pore distribution

In models F, J, and K, the total pore volumes were 6.52×10^{-3}, 6.46×10^{-3}, and 6.59×10^{-3} mm^3, respectively. Figs. 7(a), (c), and (d) show the pore distributions for these three FE models. Fig. 8(b) and Figs. 9(a) and (b) illustrate the effect of the pore location on the maximum principal stress. The highest stress concentration in model K occurs at point *A* (see Fig. 9(b)), located in the narrow region between the pore and the specimen surface. At point *A*, the stress concentration factor is 5.24, which is greater than the stress concentration factor of 4.32 in model F. However, owing to the smaller sphericity of the pore in model J, the stress concentration factor in model K is smaller than that in model J.

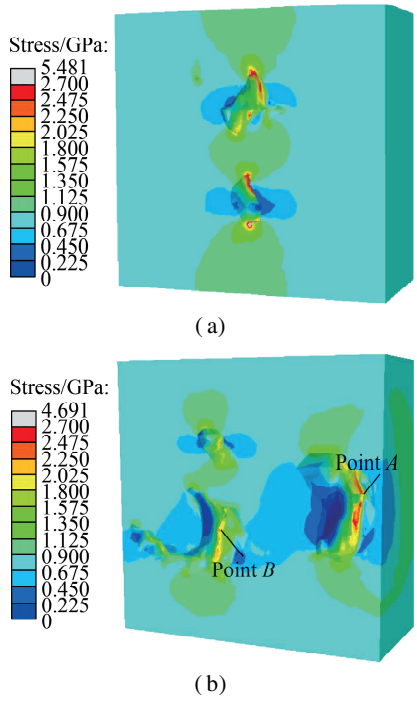

Fig. 9 Maximum principal stress distribution. (a) Model J; (b) Model K

The minimum distance from the pore or pores to the specimen surface is 5 μm (in model K). To verify the impact of the distance from a pore to the specimen surface on stress concentration, the dimensions of model K were expanded to 0.62 mm × 0.62 mm × 0.62 mm while keeping the sizes and locations of the pores unchanged. This modification increased the minimum distance from a pore to the specimen surface from 5 to 105 μm. This model was denoted as K′. The stress concentration factor obtained from the FEA simulation for model K′ is 3.64, which is less than that for model K. Moreover, the position of the maximum principal stress shifted from point *A* to point *B* (see Fig. 9(b)). The stress concentration at point *B* is caused by a sharp feature rather than proximity to the specimen surface.

4 Conclusions

1) Micropores in G20Mn5N cast steel can be classified as gas, shrinkage, and gas-shrinkage pores depending on their formation origin and morphology. The morphological characteristics of the three types of pores differ. Gas pores are almost spherical with smooth surfaces, gas-shrinkage pores have round bodies with some tail protrusions, and shrinkage pores possess elongated shapes with rough surfaces.

2) The size distribution of pores in cast steel follows a three-parameter lognormal distribution. The pore diameter threshold is approximately 62.23 μm, indicating that the detected pores in the studied cast steel are larger than this value. The clustering tendency and affinity parameters were defined to characterize the spatial correlations among the three types of pores. Understanding the spatial arrangement of micropores is useful in determining the associated mechanics and the relationship between the microstructure and properties of cast steel.

3) Pore sphericity and volume significantly affect the stress concentration in the model. Lower sphericity and larger volume of a pore result in higher stress concentration. Pores located on the specimen surface lead to greater stress concentration compared to those located inside the specimen.

References

[1] Folta M, Delić A. Quality of precipitation annealing of heat-resistant cast steel using a Taguchi analysis[J]. *Materiali in Tehnologije*, 2021, **55**(1): 83 − 88. DOI: 10.17222/mit.2020.074.

[2] Cheng J M, Gao Y Q, Yan H D, et al. Statistical analysis of nondestructive testing results of cast steel joints in civil engineering structures[J]. *Journal of Southeast University* (*English Edition*), 2022, **38**(1): 1 − 8. DOI: 10.3969/j.issn.1003-7985.2022.01.001.

[3] Bacaicoa I, Wicke M, Luetje M, et al. Characterization of casting defects in a Fe-rich Al-Si-Cu alloy by microtomography and finite element analysis[J]. *Engineering Fracture Mechanics*, 2017, **183**: 159 − 169. DOI: 10.1016/j.engfracmech.2017.03.015.

[4] Jiao H H, Yan H D, Jin H. Evaluation of mechanical properties of cast steel nodes based on GTN damage model[J]. *Journal of Southeast University* (*English Edition*), 2021, **37**(4): 401 − 407. DOI: 10.3969/j.issn.1003-7985.2021.04.009.

[5] Dorin T, Wood K, Taylor A, et al. Effect of coiling treatment on microstructural development and precipitate strengthening of a strip cast steel[J]. *Acta Materialia*, 2016, **115**: 167 − 177. DOI: 10.1016/j.actamat.2016.05.043.

[6] Yang H C, Xu F Y, Zhu D S, et al. Research on damage evolution of metal plate based on improved micropolarperidynamic model[J]. *Journal of Southeast University* (*English Edition*), 2019, **35**(3): 292 − 301. DOI: 10.3969/j.issn.1003-7985.2019.03.004.

[7] Yan H D, Jin H. Three-dimensional characteristics and morphological evolution of micro/meso pores in G20Mn5N steel castings[J]. *Acta Metallurgica Sinica*, 2019, **55**(3): 341 − 348. DOI: 10.11900/0412.1961.2018.00131. (in Chinese)

[8] Mahomed N, Kleynhans H A. Reducing shrinkage porosity in high-performance steel castings: Case of an ASME B16.34 gate valve body: Part 1—Analysis, techniques and experimental approach[J]. *International Journal of Metalcasting*, 2018, **12**(4): 919 − 926. DOI: 10.1007/s40962-018-0275-7.

[9] Gao Y X, Yi J Z, Lee P D, et al. The effect of porosity on the fatigue life of castaluminium-silicon alloys[J]. *Fatigue & Fracture of Engineering Materials & Structures*, 2004, **27**(7): 559 − 570. DOI: 10.1111/j.1460-2695.2004.00780.x.

[10] Li P, Lee P D, Maijer D M, et al. Quantification of the interaction within defect populations on fatigue behavior in an aluminum alloy[J]. *Acta Materialia*, 2009, **57**(12): 3539 − 3548. DOI: 10.1016/j.actamat.2009.04.008.

[11] Cao T S, Maire E, Verdu C, et al. Characterization of ductile damage for a high carbon steel using 3D X-ray micro-tomography and mechanical tests-Application to the identification of a shear modified GTN model[J]. *Computational Materials Science*, 2014, **84**: 175 − 187. DOI: 10.1016/j.commatsci.2013.12.006.

[12] Landron C, Maire E, Bouaziz O, et al. Validation of void growth models using X-ray microtomography characterization of damage in dual phase steels[J]. *Acta Materialia*, 2011, **59**(20): 7564 − 7573. DOI: 10.1016/j.actamat.2011.08.046.

[13] Zhao T, Li Y, Zhang C, et al. Fundamental mechanical problems in high-performance aerospace composite structures: State-of-art review[J]. *Acta Aeronautica et Astronautica Sinica*, 2022, **43**(6): 526851. DOI: 10.7527/S1000-6893.2022.26851. (in Chinese)

[14] Wu S C, Hu Y N, Yang B, et al. Review on defect characterization and structural integrity assessment method of additively manufactured materials[J]. *Journal of Mechanical Engineering*, 2021, **57**(22): 3 − 34. DOI: 10.3901/JME.2021.22.003. (in Chinese)

[15] Ziółkowski G, Chlebus E, Szymczyk P, et al. Application of X-ray CT method for discontinuity and porosity de-

tection in 316L stainless steel parts produced with SLM technology[J]. *Archives of Civil and Mechanical Engineering*, 2014, **14**(4): 608 - 614. DOI: 10.1016/j.acme.2014.02.003.

[16] Qian W J, Wu S C, Lei L M, et al. Time lapse in situ X-ray imaging of failure in structural materials under cyclic loads and extreme environments[J]. *Journal of Materials Science & Technology*, 2024, **175**: 80 - 103. DOI: 10.1016/j.jmst.2023.07.041.

[17] Wu Z K, Wu S C, Bao J G, et al. The effect of defect population on the anisotropic fatigue resistance of $AlSi_{10}Mg$ alloy fabricated by laser powder bed fusion[J]. *International Journal of Fatigue*, 2021, **151**: 106317. DOI: 10.1016/j.ijfatigue.2021.106317.

[18] Duan S, Wang P, Liu C, et al. Research progress on design, optimization and performance characterization of additive manufactured 3D lattice structures[J]. *Aeronautical Manufacturing Technology*, 2022, **65**(14): 36 - 48, 57. DOI: 10.16080/j.issn1671-833x.2022.14.036. (in Chinese)

[19] Yan H D, Jin H, Yao R G. Prediction of the damage and fracture of cast steel containing pores[J]. *International Journal of Damage Mechanics*, 2020, **29**(1): 166 - 183. DOI: 10.1177/1056789519872000.

[20] Tiryakioğlu M. On the relationship between statistical distributions of defect size and fatigue life in 7050-T7451 thick plate and A356-T6 castings[J]. *Materials Science and Engineering*: *A*, 2009, **520**(1/2): 114 - 120. DOI: 10.1016/j.msea.2009.05.005.

[21] Su X, Mao J X, Wang H, et al. Automatic identification of modal parameters of long-span bridges considering uncertainty[J]. *Journal of Southeast University* (*Natural Science Edition*), 2023, **53**(5): 850 - 856. DOI: 10.3969/j.issn.1001-0505.2023.05.012. (in Chinese)

[22] Balasundaram A, Gokhale A M. Quantitative characterization of spatial arrangement of shrinkage and gas (air) pores in cast magnesium alloys[J]. *Materials Characterization*, 2001, **46**(5): 419 - 426. DOI: 10.1016/s1044-5803(01)00141-3.

G20Mn5N 铸钢中的微细观孔洞及其对应力分布的影响

闫华东　靳　慧

(东南大学土木工程学院,南京 211189)
(东南大学江苏省工程力学分析重点实验室,南京 211189)

摘要:为了准确分析铸造缺陷的影响,基于高分辨率三维 X 射线断层成像技术,对铸钢中的微细观孔洞信息进行统计,根据微细观孔洞的成因和形态,将其分为气孔、缩孔和气缩孔,并通过定义聚集趋势和亲和参数对这 3 类孔洞之间的空间关联性进行表征.此外,将通过 X 射线断层扫描获得的三维微细观孔洞信息映射到有限元分析软件中,用于预测微细观孔洞的形态、尺寸和分布对应力分布的影响.研究发现:铸钢材料中的细观缺陷会存在一些局部半径较小的拐点,而这些拐点正是引起应力集中的主要原因,因此不能将细观缺陷简化为理想孔洞;缺陷的圆整度和体积均对模型的应力集中有较大影响,缺陷圆整度越小、体积越大,引起的应力集中越大;铸钢件内部缺陷具有全局分布特征,缺陷位于试样表面时相较于其位于试样内部时,会导致更大的应力集中.

关键词:铸钢;微细观孔洞;X 射线断层扫描;三维重建;有限元分析
中图分类号:TU512.91